Combustion and Flame 195 (2018) 267–281

Contents lists available at ScienceDirect

Combustion and Flame

journal homepage: www.elsevier.com/locate/combustflame

Sooting limits of non-premixed counterflow ethylene/oxygen/inert flames using LII: Effects of flow strain rate and pressure (up to 30 atm)

Brendyn G. Sarnacki, Harsha K. Chelliah[1,*]

Department of Mechanical and Aerospace Engineering, University of Virginia, Charlottesville, VA 22904-4746, USA

ARTICLE INFO

Article history:
Received 8 November 2017
Revised 20 March 2018
Accepted 22 March 2018
Available online 14 April 2018

Keywords:
Soot
Laser Induced Incandescence (LII)
Ethylene-air
Counterflow flames
High-pressure

ABSTRACT

An absolute irradiance-calibrated Laser Induced Incandescence (LII) technique and a standard particle image velocimetry (PIV) technique were utilized to collect quantitative data on soot volume fraction and corresponding flow strain rates of diluted ethylene-air non-premixed counterflow flames. Pressures up to 30 atm were explored with increasing dilution with nitrogen or helium to minimize flow strain limits at which incipient soot was detected and to maintain the flame in laminar mode. For weakly strained flames considered, the species and velocity boundary conditions were used to predict the gas-phase flame structure (e.g., temperature and major species). The predicted gas properties, together with soot particle temperature decay rate measured by two-color pyrometry were used in the LII heat transfer model to extract the effective soot particle size and particle number density. Estimates of global activation energy of incipient soot yield with pressure indicated a sudden change around a pressure of 20 atm, which may be attributed to a shift in soot nucleation and growth pathways.

1. Introduction

Over the last five decades, counterflow laminar flames have been extensively utilized to better understand the non-equilibrium processes occurring in flames. These included investigations about fundamental coupling mechanisms between finite-rate chemistry and transport, and efforts aimed at developing chemical kinetic models capable of simulating realistic flames or flamelets subjected to varying flow strain rates (see for example [1–14]). In addition, considerable literature exists on counterflow sooting flames (see for example [15–31]), but only a handful of studies have focused on pressure effects [32–35]. Despite the many benefits of counterflow flame geometry, the application of probe-based diagnostic techniques to extract flame structure data can introduce large uncertainties due to flame displacement and local quenching of reactions, especially in high-pressure flames. Similarly, the non-intrusive methods used for soot diagnostics in counterflow flames can have inherent uncertainties.

Several studies have used probe-based techniques to measure temperature, species, and soot characteristics in counterflow flames, ranging from incipient to heavily sooting flames [21,22,34–37]. For example Gomez and co-workers [34,35] used thin-filament pyrometry and achieved favorable spatial resolution of temperature up to 30 atm, while quartz micro-probe sampling with GC analysis was used to resolve species profiles across the flame structure, including large PAH molecules. Other researchers [21,22,36] have also used micro-probe sampling methods to quantify key soot precursor species in counterflow flames, which are critical for detailed model development work [19,38]. The majority of probed based investigations have been performed at low strain rates and atmospheric pressure conditions to achieve reasonable spatial resolution while minimizing the effects of flow disturbance by probe sampling.

In non-intrusive methods, laser extinction and scattering techniques have been used to quantify soot volume fraction and particle size in counterflow flames. In particular, Law and co-workers [17,18,32] used laser scattering signal to identify the “sooting limit,” the critical strain rate at which soot inception was observed in ethylene-air non-premixed counteflow flames. Kang et. al [20] also used a laser scattering method to analyze the effects of flame location within the mixing layer on soot formation. In addition, they reported measurements of gas temperature using the coherent anti-Stokes Raman Scattering (CARS) approach, which is important in LII model analysis. In subsequent work by Chung and co-workers [20,31], LII methodology was used to quantify the soot

* Corresponding author.
E-mail address: harsha@virginia.edu (H.K. Chelliah).
[1] Current address: Department of Engineering, Maine Maritime Academy, Castine, ME 04420.

https://doi.org/10.1016/j.combustflame.2018.03.029
0010-2180/

volume fraction to understand the synergistic effects of different fuel mixtures. Based on soot volume fraction dependence on the oxidizer mole fraction variation, they reported an overall activation energy for soot growth of 154 kJ/mol, comparable to 130 kJ/mol reported by Du et al. [32]. However, no attempt was made to maintain the stoichiometric mixture fraction (Z_{st}) as the oxidizer mole fraction was varied. Since the relevant scalar dissipation rate can vary with Z_{st} and can affect the local residence time, both the soot yields and estimated global activation energies can have contributions due to variations of flame location within the mixing layer.

The non-intrusive line-of-sight laser extinction method used for soot diagnostics in counterflow flames can suffer from flame curvature effects, while the LII signal can be affected by contributions from laser induced fluorescence (LIF) due to the presence of PAH molecules in the flame. Considerable effort has been devoted to understanding and distinguishing the LIF contributions from measured LII signal depending on the laser excitation wave length, laser fluence, and gated intensifier delay time for a range of flame conditions (see for example [39–46]). In particular, for a 266 nm ps laser excitation, Ossler et al. [40] investigated the effects of temperature and selected PAH molecules (naphthalene, fluorene, anthracene, and pyrene) on emitted fluorescence spectra. They reported a slight red-shift of the spectra when temperature was increased from 400 K to 1200 K, while the lifetime of the fluorescence of all PAH molecules analyzed was reduced to less than 2 ns at 1200 K. Similar results on fluorescence lifetime have been reported by Faust et al. [45] for naphthalene heated to a temperature of 1100 K and pressure of 10 bar, and in varying concentrations of N_2, O_2, and CO_2. To understand the fluorescence signal at different excitation wave lengths (from 266 to 680 nm), Beajaoui et al. [46] performed a careful spectroscopic investigation of atmospheric pressure methane-air premixed and non-premixed sooting flames with a low laser fluence of 0.020 J/cm^2. The results have shown that at 532 nm excitation, the peak fluorescence signal is observed at about 550 nm, with roughly an order of magnitude less on the wings, e.g., at 450 and 650 nm as considered in this work. To understand the impact of laser excitation wavelength of 532 nm on LIF, Goulay et al. [42] investigated emission spectra from a Santoro diffusion flame burner for laser fluences varying from 0.15 to 0.5 J/cm^2. For low laser fluences below 0.2 J/cm^2, it was found that the spectra displayed a predominantly broadband distribution and the signal was primarily due to LII. Based on narrow bandpass signals at 450 and 750 nm, they concluded that LII signal from 532 nm laser excitation with fluences below 0.2 J/cm^2 was adequate to characterize soot in flames.

Irrespective of above detailed LIF/LII investigations, it is clear that laser excitation wavelengths above 650 nm are ideal for LII (eg., 1064 nm excitation), including for a broad range of flame temperature, laser fluence, and intesifier delay timing. However, the data also suggests that for gas temperatures above 1000–1100 K with LIF lifetimes of the order of 2–10 ns, a laser excitation wave length of 532 nm with a fluences below 0.2 J/cm^2 is capable of minimizing the LIF contributions to the LII signal. Lower laser fluence further implies that the peak soot particle temperature remains below the sublimation temperature during laser excitation, minimizing the probability of contributions from C2-swan band emissions. Since an integral part of counterflow flames investigated here requires accurate characterization of the flow velocity across the flame structure, it was convenient to use the 532 nm wavelength for both soot (LII) and velocity field (PIV) measurements. Specifically, low laser fluences of approximately 0.1 J/cm^2 were used to collect LII signal from high-pressure, counterflow non-premixed ethylene/oxygen/inert(nitrogen or helium) flames. The filtered signal at 650 nm (10 nm FWHM) was used to characterize the soot volume fraction (f_v), while a two-color pyrometry approach was used to obtain particle temperature. Measured soot volume fraction was used to characterize the sooting limits of ethylene/oxygen/inert non-premixed flames, for pressures up to 30 atm. Analysis of the particle temperature decay over 70 ns (starting from the peak laser energy) allowed extraction of the effective particle size (d_p) from the analysis of the LII heat transfer model.

2. Experimental configuration

A non-premixed counterflow burner designed to operate at both atmospheric and elevated pressures was used to conduct all the experiments. The co-annular nozzles employed in the high-pressure burner were designed to minimize the formation of Taylor–Görtler vortices and the boundary layer growth in the converging section [47]. The inner nozzle exit diameter was selected to be 6.5 mm with an area ratio of 19.1. Inert flows of nitrogen (or helium for pressures above 14 atm) were introduced through the outer annuli to prevent secondary flames in the enclosed chamber. The nozzles were mounted vertically in the chamber, with spacers providing the ability to vary the nozzle separation distance. However, a fixed nozzle separation of 5.45 mm was used for this study. Four two inch windows arranged symmetrically on the transverse plane with respect to the axis of the nozzles, allowing access for LII and PIV diagnostics and viewing of the flame. The one inch thick fused silica windows were hydro-tested to a pressure of 150 atm, while the chamber itself was hydro-tested to a pressure of 200 atm using aluminum blanks (see Appendix A for further details of the high-pressure burner). In experiments, the oxidizer, fuel, and inert gases were metered and controlled by a series of mass flow controllers (Sierra model 100 with a factory calibrated accuracy of ±1% of full scale and repeatability of ±0.2% of full scale, including linearity at operating conditions) interfaced with a LabView data acquisition program. The chamber operating pressure was regulated via a Stravalve back-pressure regulator controlled by a stepper motor through LabView. For the case of atmospheric pressure data, the back-pressure regulator was removed.

LII measurements utilized a New Wave Research Solo III 50 mJ, 532 nm, pulsed (duration 8 ns FWHM) dual head Nd:YAG laser with collimated and apertured Gaussian sheet optics (adjustable height, ~250 μm width FWHM). Only one laser head was used for LII measurements. Laser fluence was controlled by adjusting the energy output of the flash lamp with excellent control of the beam shape and laser sheet intensity (see Section 4.4 below). A peak laser fluence of 0.098 J/cm^2 was used for LII experiments from 1 to 8.45 atm. The peak fluence was increased to 0.11 J/cm^2 from 14–30 atm to overcome losses in LII signal due to enhanced heat conduction. These low fluences were chosen to minimize contributions from PAH molecules while maximizing incandescent signal in the low fluence regime. The soot particle incandescent signal was collected through a Nikon micro-Nikkor 105 mm lens, 450 nm and 650 nm bandpass filters (10 nm FWHM), LaVision Intensified Relay Optics (IRO), and a LaVision Imager ProX4M 2048×2048 pixel CCD camera. The bandpass filters were interchanged by using a motorized filter wheel built into the optical assembly. The equipment was controlled via Davis 7.2 and LaVision SootMaster software through a programmable timing unit with 10 ns resolution. The PIV system utilized the same laser and CCD camera with a Nikon micro-Nikkor 200 mm lens and 532 nm bandpass filter (10 nm FWHM). LaVision FlowMaster software controlled PIV data collection and processing.

The general experimental procedure adopted is as follows. The camera and laser sheet were aligned perpendicularly, focused, and centered on the air nozzle exit axis of symmetry as shown in Fig. 1. Here, the air nozzle exit plane is identified by $z = +L/2$ while the fuel nozzle exit plane is identified by $z = -L/2$, with z indicating the axis of symmetry coordinate and L the nozzle sep-

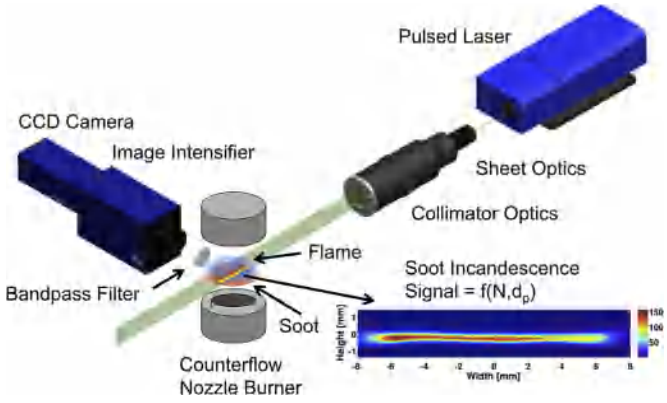

Fig. 1. Schematic and general layout of the absolute irradiance calibrated LII system. The same configuration applies to PIV without the image intensifier. The insert shows the typical image of 500 LII signals.

aration distance. Opposed non-premixed fuel, oxidizer, and inert gas dilution streams were introduced via the inner nozzles, with momenta balanced ($\rho_{ox}v_{ox}^2 = \rho_{fuel}v_{fuel}^2$). A co-flow of nitrogen or helium was introduced through the outer annulus of each nozzle with the same momentum balance. For a selected global strain rate (a function of inverse flow residence time), defined by $a_g = 4v_{ox}/L$, a LabView interface automatically assigned all flow meter settings. Here, v_{ox} is the estimated oxidizer-stream velocity determined by the ratio of the volume flow rate to nozzle cross sectional area. Once the chamber pressure was stabilized near the desired pressure, the mixture was ignited with a spark, and a stable planar axisymmetric flame was produced between the counterflow nozzles. For high pressure experiments beyond 8 atm, the burner was ignited at a lower pressure (around 6 atm) and ramped up to the desired operating pressure. A global strain rate was chosen within the sooting regime of the given fuel-oxidizer mixture, and LII image samples were collected from heated soot particles excited by the laser and filtered through the 450 nm and 650 nm bandpass filters, with an exposure time of 10 ns dictated by the intensifier gate. The IRO delay time was varied to collect gated signals temporally as the particle temperature decayed in order to characterize soot particle size.

The incandescence signal corresponding to peak particle temperature at the peak of the laser pulse was characterized as the soot volume fraction at intensifier delay time of $t = 0$. In addition, incandescence signal at intensifier delay times of $t = 20$ ns were also reported. In order to achieve sufficient signal, samples of five hundred LII images were collected at any intensifier delay time and averaged. Similarly, for characterizing flow residence time in the sooting regime, five hundred PIV images were collected and processed using Davis 7.2 and the FlowMaster software to obtain mean and RMS 2D velocity data. For the present steady laminar flames, the validity of such ensemble averaging has been previously verified via PIV measurements [12].

3. Predicted flame structure solution with measured velocity boundary conditions

The LII analysis requires information about local gas temperature and other physical properties. In the absence of a viable experimental method, for example CARS for temperature and species measurements, the present hybrid approach relies on the modeled gas-phase flame structure data. In particular, for low strain rates near sooting laminar flames as considered in this study, e.g., far from extinction limits, the molecular mixing and thermo-chemistry primarily control the flame structure solution. As shown in previous investigations, the mixing layer thickness can be well characterized by knowing the nozzle exit velocities and the gradients from PIV measurements [12,14]. Thus, by implementing the experimentally measured flow velocity boundary conditions, together with the most recent compilation of thermochemical, transport, and finite-rate chemical kinetic parameters [48], a quasi one-dimensional numerical solver [10] was employed to compute gas-phase properties of diluted ethylene-air flames considered here. Figure 2 shows the typical predicted flame structure along the axis of symmetry obtained for pressures of (a) 1 atm and (b) 30 atm, for a local flow strain rate of 200 s^{-1}. At high pressure, the high momenta of the two jets due to increased bulk density leads to a thin mixing layer and a flame, as evident from this figure. As a result, probing high pressure flames are rather challenging, with much lower spatial resolutions. Note that the peak temperature sits to the right of the stagnation plane for the fuel and oxidizer compositions selected. It will be shown later that the peak LII signal will occur to left of the peak flame temperature and spill over to the left of the stagnation plane due to thermophoresis effects. The predicted soot precursor species, e.g., acetylene and popargyl, are also shown in Fig. 2, but their uncertainties can be high depending on the accuracy of the chemical kinetic model. It should be noted that understanding the uncertainties of the chemical ki-

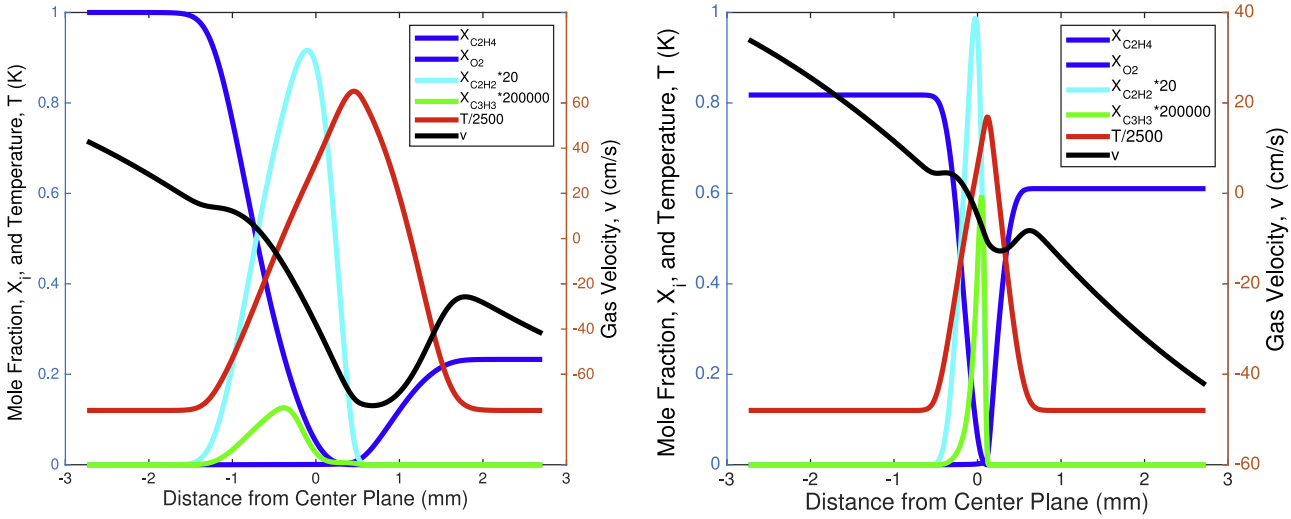

Fig. 2. Typical example of the predicted ethylene/oxygen/inert non-premixed flame structures at pressures of (a) 1 atm (undiluted) and (b) 30 atm (diluted with helium), for a local strain rate of 200 s^{-1} with velocity boundary conditions (axial velocity and gradient) imposed from measured PIV data.

netic model and transport parameters is beyond the scope of this work but have been explored using Monte Carlo simulations [49].

4. LII methodology

The general LII methodology of determining soot volume fraction, particle temperature, and number density is well established and described elsewhere (see for example [50–52]). However, obtaining quantitative data requires careful calibration, and the procedures adopted here for steady laminar counterflow flames with barely sooting conditions are described below. First, the primary soot particles formed are assumed to be in spherical shape having an effective monodispersed size, i.e., with minimal aggregate formation. Under these conditions, the local soot volume fraction can be written as $f_v = (\pi N_p d_p^3)/6$, where N_p is the local primary soot particle number density and d_p is the local effective monodispersed particle size. Thus, by knowing f_v and d_p, the soot particle number density can be readily evaluated. The soot volume fraction is obtained using the irradiance-calibrated approach proposed by Snelling et al. [53], where the soot volume fraction at a filtered incandescence wave length (λ_i) is given by,

$$f_{v,i} = \frac{I_{LII}(\lambda_i)\pi\eta_i}{\Omega A_e I_m(\lambda_i)}. \tag{1}$$

Here, $I_{LII}(\lambda_i)$ is the measured incandescent signal evaluated at the peak particle temperature or at some delayed intensifier time setting (e.g., +20 ns from the peak with a gate width of 10 ns) to minimize the LIF contributions, $I_m(\lambda_i)$ the modeled incandescent signal, η_i the calibration factor, Ω the measured solid angle of the detector optics, and A_e the calibrated area of one pixel from a spatial calibration of the detection device in the configuration used to conduct LII experiments. A non-spectral soot volume fraction can be defined as the average from the two detection wavelengths, $f_v = (f_{v,1} + f_{v,2})/2$, or simply the value at a specific wavelength at which LIF contributions are minimal. However, proper choice of weight factors can be used in the model fitting routine results in good convergence between the two signal wavelengths, with the measured volume fractions being nearly identical.

The hybrid experimental-modeling approach adopted here also requires co-optimization, for example determination of $I_m(\lambda_i)$ in Eq. (1) by solving for the LII heat transfer model. Procedures adopted to determine η_i, $I_m(\lambda_i)$, and laser heated soot particle temperature (T_{LII}) are discribed below.

4.1. Absolute irradiance calibration factor of ICCD camera (η_i)

Following the calibration approach proposed by Snelling et al. [53], a light source of known spectral irradiance (model RS-10D from Gamma Scientific) was used for calibration of the detection system. A sample of five hundred images of the irradiance incident on the intensified CCD from the calibrated light source were collected over 10 ns gate widths and through two 10 nm bandwidth bandpass filters centered at 650 nm and 450 nm. Calibration data were also collected over three different separation distances between the calibrated light source and the detector (irradiance incident on the detector scales with the inverse-square law of distance and the calibrated physical area represented by one pixel on the CCD). The signal counts were related back to an irradiance scale by a calibration factor η_i at the ith wavelength,

$$\eta_i = \frac{A_c I_c(\lambda_i)\Delta t_g}{I_{LS}}, \tag{2}$$

where I_{LS} is the averaged energy response from the calibrated irradiance light source imaged onto the CCD, A_c the calibrated area of one pixel of the CCD camera to image dimensions from a spatial calibration of the detection device in the configuration used to conduct radiometric calibrations, Δt_g the temporal gate width of the image intensifier, and $I_c(\lambda_i)$ the known absolute spectral irradiance at the bandpass filter center wavelength λ_i from the calibrated light source. The procedure results in a calibration for direct measurement of soot volume fraction according to the incandescent emission of soot particle radiation from Plank's law if the laser heated soot particle temperature (T_{LII}) is known.

4.2. Particle temperature from LII signal (T_{LII})

The experimental soot particle temperature was extracted from a combination of two-color pyrometry and incandescent signal decay. For example, knowing the peak incandescence signal ($I_{LII,\,p}(\lambda_i)$) at a wave length of λ_i, the peak particle temperature ($T_{LII,\,p}$) can be evaluated by the following two-color pyrometry equation [53],

$$T_{LII,p} = \frac{hc}{k_B}\left(\frac{1}{\lambda_2} - \frac{1}{\lambda_1}\right) \Big/ \ln\left[\frac{I_{LII,p}(\lambda_1)E(m)\eta_1\lambda_1^6}{I_{LII,p}(\lambda_2)E(m)\eta_2\lambda_2^6}\right]. \tag{3}$$

Here, h is the Planck constant, c the speed of light, k_B the Boltzmann constant, $E(m) = -\mathrm{Im}[\frac{m^2-1}{m^2+2}]$ the absorption function of soot (a function of the complex index of refraction $m = n + i\kappa$), and λ_1 and λ_2 the center detection wavelengths of 650 and 450 nm, respectively. While the complex index of refraction is a function of wavelength, both 650 nm and 450 nm wavelengths are found to fall near a trough in the curve for the refraction index of soot based on dispersion theory. The absorption function is therefore assumed to be constant between the two detection wavelengths. The literature reports values for E ranging from 0.18 to 0.4, depending on radiation from incipient or mature soot, as well as other factors involving the flow field [51,54]. In this work, a constant $E(m) = 0.3$ was assumed, consistent with previously reported counterflow flames [29]. The resulting temporal decay of particle temperature ($T_{LII}(t)$) after the peak particle temperature was determined here by the using Planck's law for radiation, with the filtered signal at $\lambda_1 = 650$ nm,

$$T_{LII}(t) = \frac{hc}{\lambda_1 k_B \ln\left[\frac{I_{LII,p}(\lambda_1)}{I_{LII}(t;\lambda_1)}\exp^{(hc/\lambda_1 k_B T_{LII,p})} - \frac{I_{LII,p}(\lambda_1)}{I_{LII}(t;\lambda_1)} + 1\right]}. \tag{4}$$

The temperature decay calculated from Eq. (4) was tested against the use of Eq. (3) exclusively and the results show that Eq. (4) yields more accurate values due to the strong signal decay at 450 nm wavelength with decreasing temperature. Hence, Eq. (3) was used to determine the peak particle temperature $T_{LII,\,p}$ and Eq. (4) was used to determine the temporal decay of the soot particle temperature.

4.3. Modeled incandescence signal ($I_m(\lambda_i)$) and primary particle size (d_p)

In order to determine primary particle size, the experimental particle temperature decay curve determined by Eqs. (3) and (4) must be fitted to the results of an LII heat transfer model representing the same particle temperature decay. With a LII heat transfer model solution (see Appendix B for details), the modeled incandescent signal is given by,

$$I_m(t;\lambda_i) = \frac{24\pi^2 E(m)}{\lambda_i}\int_t^{t+\Delta t_g}\int_{-\infty}^{\infty} B_T(t,y;\lambda_i)\,dy\,dt, \tag{5}$$

where B_T is the spectral radiance. The modeled incandescence signal is integrated over the laser sheet width profile shown in Fig. 3(b) and Δt_g the intensifier gate time. From Planck's law, B_T can determined from,

$$B_T(t,y;\lambda_i) = \frac{2\,hc^2}{\lambda_i^5}\left[\exp\left(\frac{hc}{\lambda_i k_B T_{p,i}(t,y)}\right) - 1\right]^{-1}. \tag{6}$$

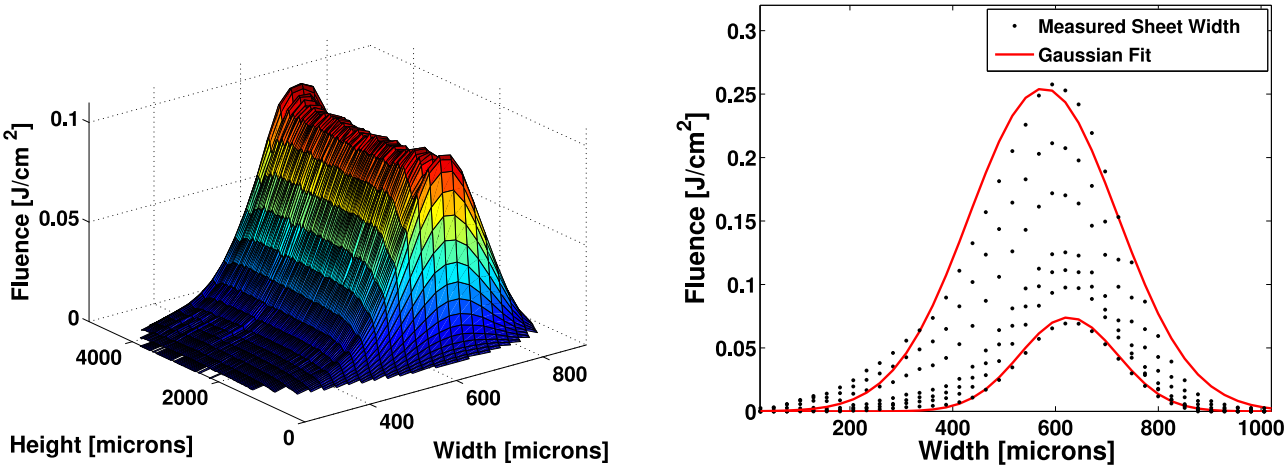

Fig. 3. (a) 2D profile of laser sheet used in LII and (b) calibrated laser sheet-width profiles for several fluence settings (black dots) with Gaussian profile fits (red lines). (For interpretation of the references to color in this figure legend, the reader is referred to the web version of this article.)

Since the particle temperature varies over the intensifier gate width of 10 ns, in Eq. (5) the contribution of spectral radiance term is calculated using the temperature obtained by integrating the internal energy conservation equation ($T_{p,i}(t, y)$) as described in Appendix B. Once $I_m(t; \lambda_i)$ is determined from Eq. (5) or any other procedure, an alternate modeled particle temperature ($T_m(t)$) can be evaluated using the two-color pyrometry equation,

$$T_m(t) = \frac{hc}{k_B}\left(\frac{1}{\lambda_2} - \frac{1}{\lambda_1}\right) \Big/ \left[\ln\left(\frac{I_m(t;\lambda_1)\lambda_1^6}{I_m(t;\lambda_2)\lambda_2^6}\right)\right]. \tag{7}$$

The fitting procedure matches experimental peak temperature (T_{LII}) with modeled peak temperature (T_m) while also determining particle size (d_p) by iterative weighted least-squares minimization of the modeled and experimental particle temperature decays. The fitting procedure utilizes a two parameter fit: d_p and a placeholder variable to adjust laser fluence to match peak temperatures. With this approach, careful determination of absolute laser fluence is unnecessary, minimizing issues of beam steering on the laser source. During fitting, the error in the peak temperatures are preferentially matched with a weight factor of 6, providing good convergence of the volume fraction measurement between the 650 nm and 450 nm filters while also resulting in a particle size fit within a few percent of an unweighted regression.

4.4. Laser beam profile and fluence calibration

An accurate LII model also requires careful spatial characterization of the excitation laser source. The measurements were conducted with a Thorlabs BC106-VIS CCD beam profiler and a total laser pulse energy transfer calibration from a Scientech AC2501 Astral Calorimeter with 3% documented uncertainty. Measurements from five hundred successive laser pulses were recorded for a range of laser power settings covering the parameters defined by low to high fluence LII. Figure 3(a) shows the 2D profile of the laser sheet, while Fig. 3(b) shows a plot of the laser sheet width as a function of calibrated laser fluence. The beam sheet appears to be largely Gaussian, with some minor Fresnel diffraction noticeable at the two ends. The lowest fluence profiles exhibited the best Gaussian fits. Collimation of the sheet minimized the diffraction pattern. The beam sheet profile along the center in height is clearly consistent and was configured such that the soot layer was uniformly heated from this constant profile center in height (approximately 2.5 mm). Shot to shot variation of the order of 10% was recorded and assumed negligible over a five hundred sample average. The fluences ranging from 0.08 to 0.26 J/cm^2 are shown in Fig. 3(b), however, LII experiments were performed with fluences of 0.098 J/cm^2 at 1–8.45 atm and 0.11 J/cm^2 at 14–30 atm. Note that the beam sheet width must be well characterized for accurate LII measurements due to integration in Eq. (5) while the determination of absolute laser fluence is unnecessary due to the fitting procedure used. Beam steering is effectively minimized because the laser sheet profile (Fig. 3(b)) is perpendicular to flame temperature and density gradients.

5. Thermophoretic velocity of soot particles

In PIV measurements, the PIV seed particles precisely follow the gas flow in the cold region, while the nano-sized soot particles can have a different velocity from the gas due to the steep temperature gradients found within the thermal mixing layer [19]. This difference is attributed to the thermophoretic forces acting on the particle. Because of the broad variation of the Knudsen number around the soot particles, i.e., from the free molecular to continuum regime, a thermoporetic force model proposed by Talbot et al. [55] and validated for $0 < Kn < \infty$ with less than 20% uncertainty is implemented here,

$$F_T = -\frac{12\pi\mu\nu r_p C_s\left(\frac{\kappa}{\kappa_s} + C_t\frac{\lambda}{r_p}\right)\nabla T}{T\left(1 + 3C_m\frac{\lambda}{r_p}\right)\left(1 + 2\frac{\kappa}{\kappa_s} + 2C_t\frac{\lambda}{r_p}\right)}. \tag{8}$$

The above formulation assumes a thermal accommodation coefficient α_T of unity with minimal error on the predicted value of F_T (see [55]). With the assumption that the thermophoretic force is balanced by the Stokes drag force, and with the Millikian formula for the drag force given by,

$$F_v = -\frac{6\pi\mu\nu_T r_p}{1 + \frac{\lambda}{r_p}\left(A + B\exp^{-Cr_p/\lambda}\right)}, \tag{9}$$

the thermophoretic velocity, ν_T, can be readily evaluated. Here, μ is the local gas mixture dynamic viscosity, ν the kinematic viscosity, κ the thermal conductivity, λ the mean free pat, T the gas temperature, ∇T the gas temperature gradient, r_p the effective radius of the soot particle, and κ_s the particle thermal conductivity. Optimum values of the thermal slip coefficient $C_s = 1.17$, temperature jump coefficient $C_t = 2.18$, and momentum exchange coefficient $C_m = 1.14$ were determined from kinetic theory and provided in the work by Talbot et al. [55]. Coefficients A, B, and

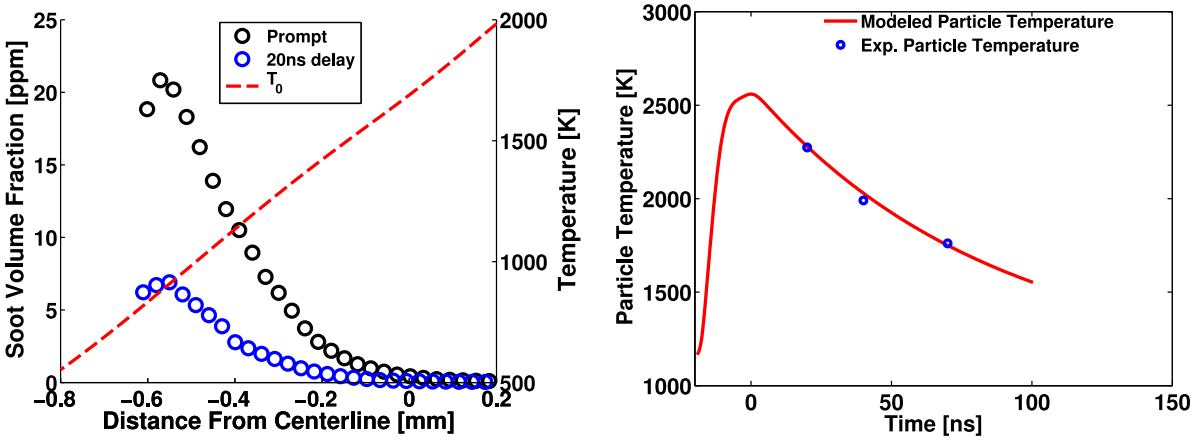

Fig. 4. Measured soot volume fraction (f_v) and particle temperature decay (T_p) for an undiluted ethylene-air non-premixed flame at 2 atm and $a_l = 187$ s^{-1}. f_v data are shown for two different intensifier delay times, while T_p decay data is shown at z=−0.4 mm.

C in the Millikan drag formula were given as 1.2, 0.41, and 0.88, respectively. With mean free path of the local gas mixture $\lambda = (\mu/\rho)\sqrt{\pi\overline{W}/(2RT)}$, the gas mixture viscosity $\mu = \kappa\overline{W}/(fR(\gamma - 1))$ (in terms of thermal conductivity for polyatomic gases and the Eucken correction formula $f = (9\gamma - 5)/4$), and the equation of state of ideal gas $\rho = p_0\overline{W}/RT$ yields the following expression for thermophoretic velocity v_T,

$$v_T = -\frac{2\kappa(\gamma-1)C_s(\frac{\kappa}{\kappa_s} + C_t\frac{\lambda}{r_p})[1 + \frac{\lambda}{r_p}(A + B\exp^{-Cr_p/\lambda})]\nabla T}{fp_0(1 + 3C_m\frac{\lambda}{r_p})(1 + 2\frac{\kappa}{\kappa_s} + 2C_t\frac{\lambda}{r_p})}. \quad (10)$$

While the above expression includes pressure effects, for very high pressures, corrections must be introduced to the assumed ideal gas equation of state. Knowing v_T, the total soot particle velocity (v_p) is simply the sum of the thermophoretic velocity and local gas velocity, and is used here to identify the stagnation plane of soot particles in the counterflow field.

6. Results and discussion

With the hybrid experimental-modeling procedure described above, for an undiluted ethylene-air non-premixed flame (mole fractions at the boundaries: $X_{C_2H_4,-L/2} = 1.0$ and $X_{O_2,+L/2} = 0.21$) at a pressure of 2 atm and a local strain rate of $a_l = 187$ s^{-1}, Fig. 4 shows (a) typical soot volume fraction profile as a function of the distance normal to the flame obtained at two different intensifier gate times (0 ns and 20 ns delay from the peak) and (b) typical particle temperature decay at $z = -0.4$ mm. Here, f_v is based on Eq. (1) with the incandescence signal filtered at 650 nm (10 nm FWHM) for a laser excitation wave length of 532 nm, while T_p is based on Eqs. (3) and (4). A key unknown is the contributions from LIF of PAH molecules to the LII signal. In an investigation of LIF from PAH, Beajaoui et al. [46] showed that the signal filtered at 650 nm (near edges of the fluorescent band width) has an order of magnitude less contributions than those closer to the excitation wavelength of 532 nm and at prompt detection conditions (0 ns intensifier delay). Thus, at 20 ns intensifier delay with 0.1 J/cm^2 fluence, such contributions are assumed to be negligible because of the short lifetime of PAH molecules. In contrast, Fig. 4(a) indicates that from $z = -0.6$ to -0.4 mm with temperature varying from 800–1100 K, there is a rather significant drop in the LII signal, perhaps indicating a long lifetime effect of PAH at such low temperature regions of the flame. At high temperature region of the flame, the difference between the prompt and delayed signal is seen to slightly diminish. On the other hand, Fig. 4(b) shows a reasonable particle temperature decay, which was extracted from two-color pyrometry data and solving for the LII heat transfer model. Irrespective of the above uncertainty of LIF contributions, the soot volume fraction and particle size obtained in the present analyses are consistent with previous studies using LII with 532 nm excitation and laser extinction/scattering methods [24,29].

With the stoichiometric mixture fraction of $Z_{st} = 0.064$ and the flame anchored towards the oxidizer boundary of the mixing layer, Fig. 5 indicates that the soot particles are nucleated at a temperature of about 1500 K on the fuel-rich side of the flame ($Z > Z_{st}$). The nucleated particles are then convected towards the stagnation plane and grow continuously until they are radially convected away by the divergent flow field. Because of the thermophoretic velocity of soot particles, the gas and the soot particle velocity differ from each other, resulting in two different stagnation planes for the gas and the soot particles as indicated in Fig. 5. Also shown in the figure are soot particle sizes (d_p) determined by the LII model described above for two different intensifier delayed signals, namely 0 ns and 20 ns. Interestingly, the particle size appears to be relatively insensitive to intensifier delay since the delay time is very short in comparison to the flow residence time, which is of the order of 10 ms. The particle size growth is consistent with the increased residence time as it approaches the stagnation plane and the availability of species contributing to the growth mechanisms, i.e., C_2H_2 for HACA, C_3H_3, PAH for condensation, etc. [56].

The variations of calculated flame structures and measured soot volume fraction, size, and number density as a function of the local flow strain rate (a_l) are presented in the next section, followed by the pressure effects.

6.1. Flow strain rate effects

With the LII procedure described above, Fig. 6 shows the soot volume fraction measured at 20 ns delay from the peak signal as a function of the distance normal to the flame, for a nonpremixed ethylene-air flame at 2 atm and several flow strain rates (ranging from highly sooting flame with a_l=187 s^{-1} to weakly sooting flame with a_l = 592 s^{-1}). Also shown are the numerically calculated and normalized profiles of C_2H_2 and C_3H_3 to indicate the soot precursor formation region, normalized OH profile to indicate the radical production, oxygen consumption layer, and locations of peak gas temperature, gas stagnation plane, and particle stagnation plane. A comparison of two strain rate results show a clear reduction in peak soot volume fraction, about an order of magnitude, as the local strain rate is increased to 592 s^{-1}. As described by Du et al. [17], the limiting strain rate at which the sooting layer disappears can be identified as an appropriate sooting limit condition

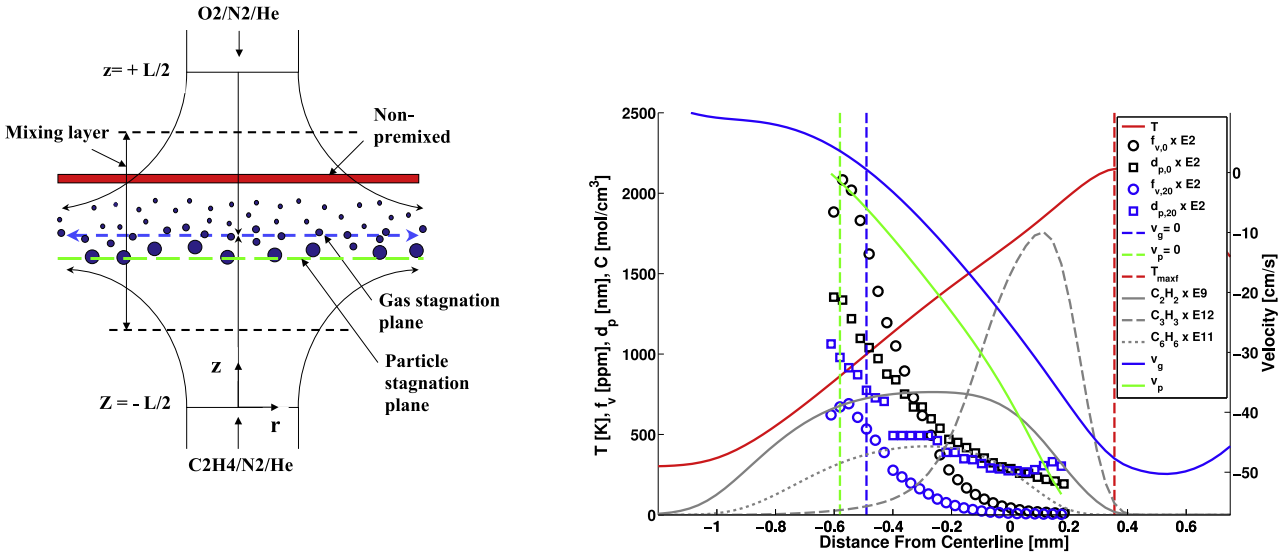

Fig. 5. (a) Illustration of the axi-symmetric counterflow field and (b) plot of calculated flame structure and the measured soot volume fraction (f_v) for an undiluted ethylene-air non-premixed flame at 2 atm and $a_l = 187\ s^{-1}$. The point of maximum flame temperature is given by the vertical dashed red line. Normalized soot precursor profiles of C_2H_2, C_3H_3, and C_6H_6 from computations are shown in grey to illustrate the sooting region. The blue solid line represents the local gas velocity with the vertical dashed blue line indicating the gas stagnation plane. The green solid line represents the local particle velocity due to thermophoresis with the vertical dashed green line indicating the particle stagnation plane. (For interpretation of the references to color in this figure legend, the reader is referred to the web version of this article.)

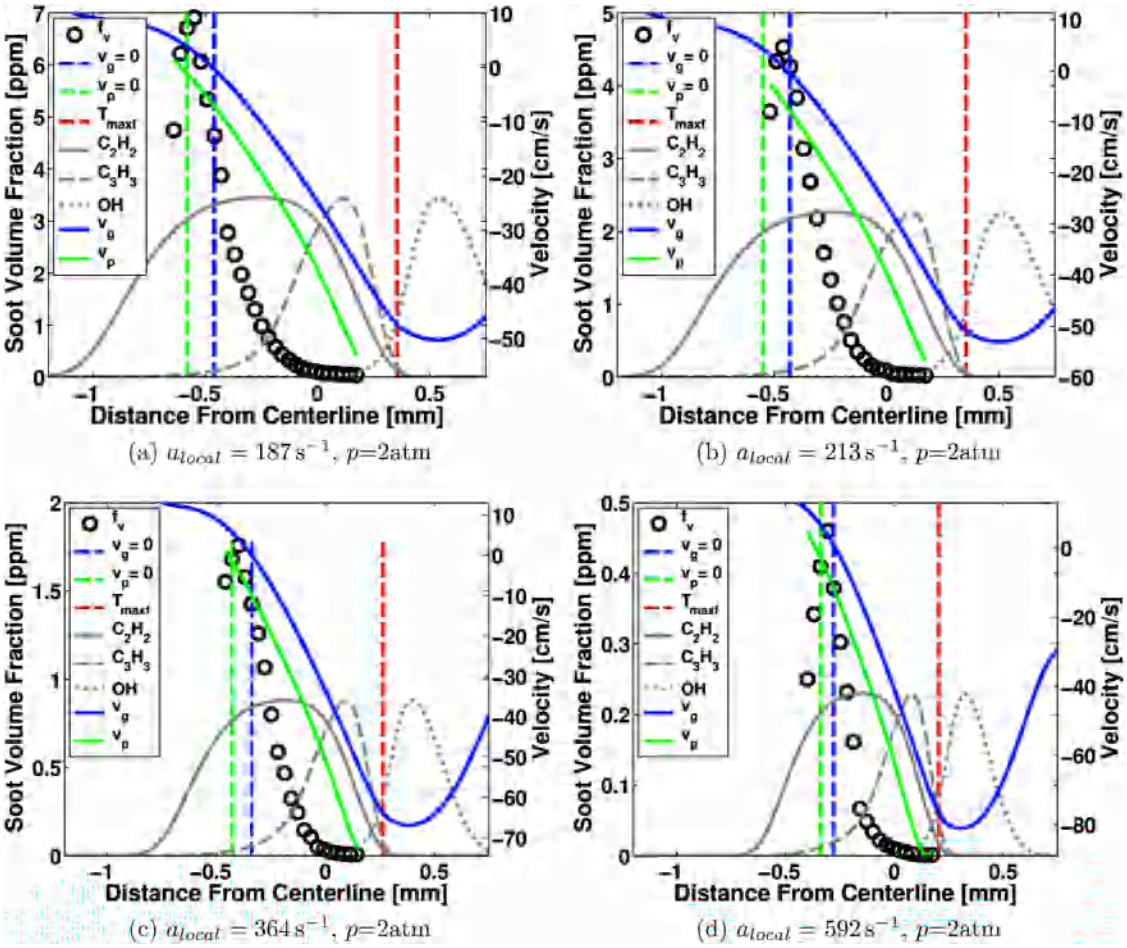

Fig. 6. Measured soot volume fraction profiles, for an undiluted ethylene-air non-premixed flame for several flow strain rates and at a pressure of 2 atm. The point of maximum flame temperature is given by the vertical dashed red line. Normalized soot precursor profiles of C_2H_2 and C_3H_3 from computations are shown in grey to illustrate the sooting region. The blue solid line represents the local gas velocity with the vertical dashed blue line indicating the gas stagnation plane. The green solid line represents the local particle velocity due to thermophoresis with the vertical dashed green line indicating the particle stagnation plane. (For interpretation of the references to color in this figure legend, the reader is referred to the web version of this article.)

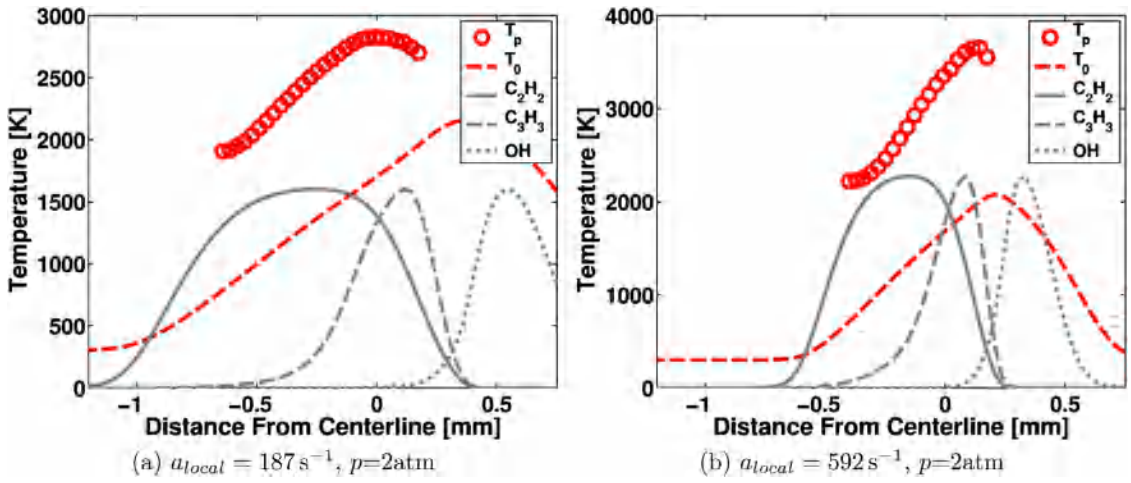

Fig. 7. Measured peak particle temperature profiles (red circles), for an undiluted ethylene-air non-premixed flame at two different flow strain rates and at a pressure of 2 atm. Also shown are the predicted gas temperature lines (dashed red line) and key relevant species. (For interpretation of the references to color in this figure legend, the reader is referred to the web version of this article.)

at local temperature, pressure, and composition. The rapid drop in soot volume fraction as the particle approaches the particle stagnation plane is consistent with previous work, and the estimated particle stagnation plane location is consistent with the estimated thermophoretic velocity [19,29]. Also evident from this figure is the reduced flame thickness with increasing strain rate, especially the soot production layer for low Z_{st} flames considered here.

Figure 7 shows the measured peak particle temperature from two-color pyrometry (solid red line) and the numerically calculated local gas temperature profile (dashed red line), for low and high strain rates of 187 and 592 s^{-1}. Similar to Fig. 6, numerically calculated and normalized profiles of C_2H_2, C_3H_3, and OH are shown to indicate the soot precursor formation region and radical production region. For all cases presented, peak particle temperatures are well below the sublimation temperature of approximately 3900–4000 K. However, at the near sooting high flow strain rate condition (592 s^{-1}) with low soot volume fraction, the evaluated particle temperature is almost 700 K greater than that of the highly sooting flame at a lower flow strain rate of 187 s^{-1}. Several factors can contribute to the difference in temperature observed. At higher strain rates, it is evident that the soot layer is closer to maximum flame temperature due to increased flow strain and thinning of the reaction zone, resulting in higher peak LII temperatures. With fixed laser fluence, attenuation of the laser energy across the flame by highly sooting low strain rate flames can lead to a reduction in soot particle temperature at the measurement plane, i.e., the axis of symmetry. In contrast, low sooting highly strained flames with no significant loss in laser energy can result in higher particle temperature. Additional factors that can lead to the observed temperature difference can be due to increased uncertainty in the particle temperature measurement at higher strain rates and changes in laser diffraction from the lensing effect of the temperature gradient in the reaction zone at different strain rates. More work is needed to carefully quantify these effects.

With the particle temperature decay data shown in Fig. 4(b), the LII heat transfer analysis (see Appendix B) can be applied to extract the particle size for all the cases considered. Figure 8 shows the estimated soot primary particle diameter profiles for two flow strain rates of 187 and 592 s^{-1} at a pressure of 2 atm. Interestingly, the peak particle size seems to be nearly invariant with the flow strain rate, while as seen in Fig. 6, the soot volume fraction decreases by an order of magnitude with the increasing strain rate. For further insight, particle residence time was calculated from start of soot nucleation to maximum soot particle size according to $t_{res} = \sum \Delta x / v_p(x)$ where Δx is a differential axial distance and $v_p(x)$ the particle velocity including thermophoresis. The results indicate that particle residence time in the flow field remains high, approximately 10 ms, regardless of changes in strain rate. This observation may be a primary factor in explaining why primary particle size remains fixed with changes in strain rate. Figure 8 also reveals that the estimated soot particle size initially decrease in size as the particles are convected from the peak flame temperature region, then start to grow again in the fuel rich region of the flame where there is abundant C_2H_2 and other soot precursor species. Previous non-premixed counterflow flame investigations with undiluted ethylene-air have shown a similar profile for aggregate size with distance across the flame, with a peak aggregate size of of 50–60 nm [29].

Once the soot volume fraction and the effective particle size are determined by LII analysis, the soot number density (N) can be readily extracted from the relationship $f_v = (\pi N_p d_p^3)/6$. Figure 9 shows soot number density profiles as a function of the distance across the flame front, for two different flow strain rates of 187 and 592 s^{-1} and a pressure of 2 atm. The peak number density is seen to decrease by a factor of about three as the flow strain rate is increased from 187 to 592 s^{-1}. The initial increase in soot particle number density as they get convected towards the stagnation plane, followed by a decrease in N, is consistent with the soot particle nucleation occurring in a less divergent region of the counterflow field followed by highly divergent flow as the stagnation plane is approached (see the illustration Fig. 5a). While the reported number densities are consistent with those reported by Wang et al. [29], it is worth noting that the uncertainty of the evaluated particle number density from above expression is the highest of all LII extracted soot quantities because of propagation of errors of two measured quantities, i.e., f_v and d_p.

6.2. Pressure effects

In addition to the low-pressure counterflow flame experiments discussed above, experiments were also performed at high-pressure conditions by using a series of back-pressure regulators (see Table 1). Although the high-pressure chamber was hydrotested up to 200 atm, the present experiments were limited to a maximum pressure of 30 atm due to the limitation of mass flow controllers available (maximum pressure of 34 atm). Experiments were performed with varying amounts of diluents in order to maintain laminar flames and reduce temperature and species

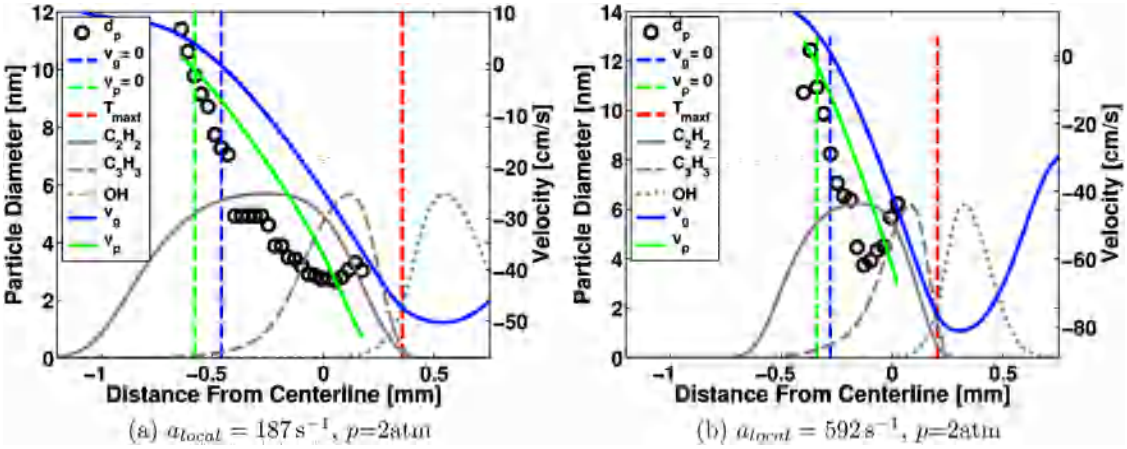

Fig. 8. Measured effective particle diameter profiles (black circles), for an undiluted ethylene-air non-premixed flame at two different flow strain rates and at a pressure of 2 atm. The blue solid line represents the local gas velocity with the vertical dashed blue line indicating the gas stagnation plane. The green solid line represents the local particle velocity due to thermophoresis with the vertical dashed green line indicating the particle stagnation plane. (For interpretation of the references to color in this figure legend, the reader is referred to the web version of this article.)

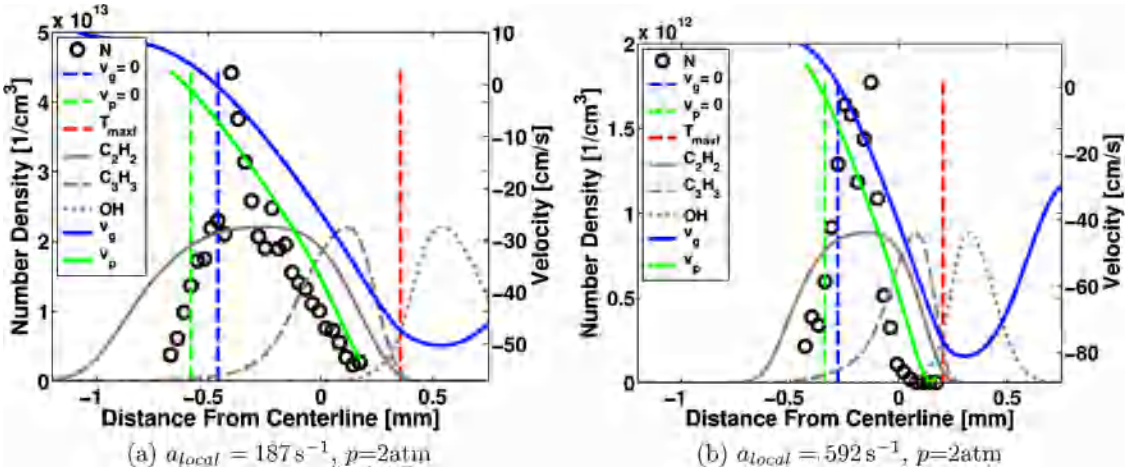

Fig. 9. Measured particle number density profiles (black circles), for an undiluted ethylene-air non-premixed flame at two different flow strain rates and at a pressure of 2 atm.

Table 1
Summary of high-pressure non-premixed counterflow ethylene/oxygen/inert mixture experiments performed, including the sooting strain rate limits and global activation energy of nucleation. Note: X_i is the fuel or oxidizer mole fraction in each stream, with remainder as the diluent.

Pressure (atm)	X_F	X_O	Diluent	Z_{st}	$(a_l)_{limit}$	$E_{a,\,nuc}$(kJ/mol)
1	1.0	0.21	Nitrogen	0.064	374	476
2	1.0	0.21	Nitrogen	0.064	798	698
4	0.5	0.21	Nitrogen	0.120	430	452
8	0.4	0.168	Nitrogen	0.120	220	1539
14	0.41	0.172	Helium	0.180	193	13976
20	0.40	0.168	Helium	0.180	218	29118
30	0.39	0.164	Helium	0.179	104	24131

gradients at high pressure. These design constraints reduced LII signal steering effects and maximized measurement resolution and accuracy. For each fixed pressure investigation, the stoichiometric mixture fraction (Z_{st}) was held constant while the flow strain rate was varied. The combination of a lower flow velocity (associated with low strain rate diluted flames) and the lower density (due to helium dilution) effectively reduced the Reynolds number, thereby maintaining high-pressure flames in laminar flame mode.

In high-pressure co-flow experiments, the soot yield or volume fraction is known to increase with increasing pressure [57]. In contrast, in the present counterflow experiments, the soot volume fraction was controlled by varying the flow strain rate (which is proportional to inverse of the residence time) and the dilution of both fuel and oxidizer streams. Figure 10 shows the measured soot volume fraction and effective soot particle diameter as a function of the distance normal to the flame front, for a diluted ethylene/oxygen/helium non-premixed flame at a pressure of 20 atm and a local strain rate of 110 s^{-1}. A comparison with the 2 atm data shown previously indicates that the maximum soot volume fraction at 20 atm and strain rate of 110 s^{-1} is similar to that of 2 atm and 592 s^{-1} flame conditions shown in Fig. 6(d), with a peak $f_v = 0.5$ ppm. In contrast, the effective peak soot particle size is seen to increase from about 12 nm at 2 atm to about 50 nm at 20 atm. This difference in particle size leads to a soot particle number density that is about two orders of magnitude lower at high-pressure conditions, implying that the soot nucleation rate is much slower at high pressure conditions. However, due to the lower strain rate of high pressure flame (at $a_l = 110$ s^{-1}), particles have sufficient time to grow to the observed 50 nm size, yielding the same soot volume fraction. It should be pointed out that at 50 nm, soot particles most likely have significant agglomeration, and the present LII analysis needs to include complex soot particle structure details as discussed in Appendix B. Furthermore, subtle differences in the local soot precursor concentrations, pressure dependent kinetic rates, and differences in flame location within the mixing layer can contribute to the differences of the soot char-

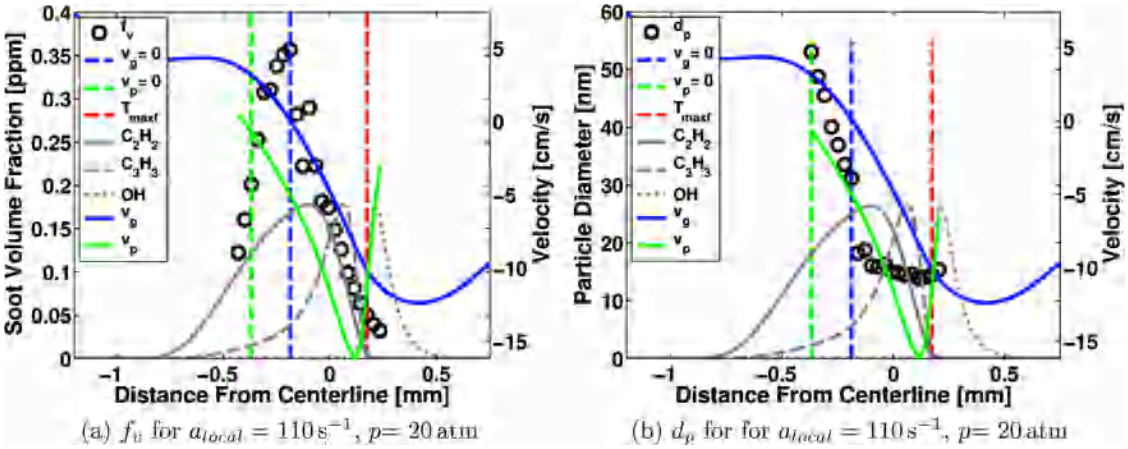

Fig. 10. Measured soot volume fraction and effective particle size profiles, for a diluted ethylene/oxygen/helium non-premixed flame at a local strain rate of 110 s^{-1} and a pressure of 20 atm.

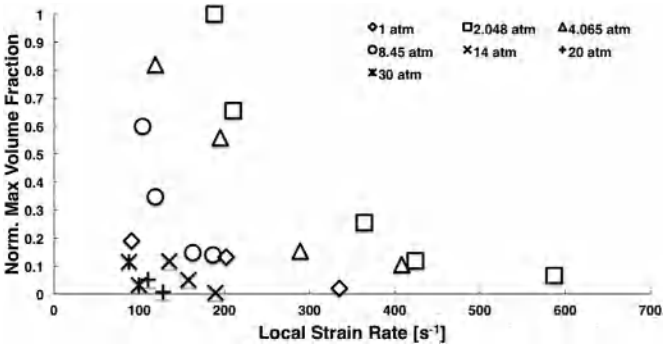

Fig. 11. Maximum soot volume fraction vs local flow strain rate, (i) no dilution for pressures 1–2 atm with Z_{st}=0.063, (ii) nitrogen dilution of ethylene for pressure 4 atm with Z_{st}=0.120, (ii) nitrogen dilution of both ethylene and oxygen streams with Z_{st}=0.120 (iii) helium dilution for pressures 14–30 atm with Z_{st}=0.18.

acteristics observed. Only a well-validated aerosol dynamic model can address these differences in greater detail.

For all the high-pressure experiments with combinations of ethylene/oxygen/diluent mixture conditions listed in Table 1, a compilation of maximum soot volume fraction vs flow strain rates is summarized in Fig. 11. The intercept with the x-axis yields the "sooting limit" for each selected pressure and composition condition, and all such limits are listed in Table 1 as $(a_l)_{limit}$. Because of the increasing slope of maximum soot volume fraction with pressure, any LIF contributions to the measured sooting limit are expected decrease with pressure. This must be verified in future experimentation by using a near IR laser excitation source, e,g. laser excitation wavelength of 1064 nm.

The number density of soot nucleated early in the counterflow flame is the key to understanding soot formation pathways. It is useful to recall that the maximum soot particle number density in counterflow flames occurs at the point where the soot particle nucleation rates are overtaken by rates of coagulation and mass loss from flow divergence. A global activation energy of soot nucleation can be extracted from the present data by assuming a global nucleation model represented by $N_{max}/t_{res} = c_{nuc}A_{nuc}e^{-E_{a,nuc}/RT_{max}}$, where N_{max} is the measured maximum number density, t_{res} the residence time to maximum number density, c_{nuc} the concentration of key species controlling soot nucleation, A_{nuc} the effective collision frequency, $E_{a,\,nuc}$ the activation energy of the global reaction, R the universal gas constant, and T_{max} the maximum flame temperature. In Fig. 12a, N_{max}/t_{res} is plotted as a function of $1/RT$, for pressures from 1 to 30 atm and for a range of local strain rates at each pressure. Residence time from start of soot nucleation to maximum number density was calculated by $t_{res} = \sum \Delta x/v_p(x)$ where Δx is a differential axial distance and $v_p(x)$ the particle velocity including thermophoresis. The slope of each line shown in Fig. 12a corresponds to a global activation energy for nucleation at a selected pressure, with flame temperature variations arising from variation of the imposed flow strain rates at a constant Z_{st}.

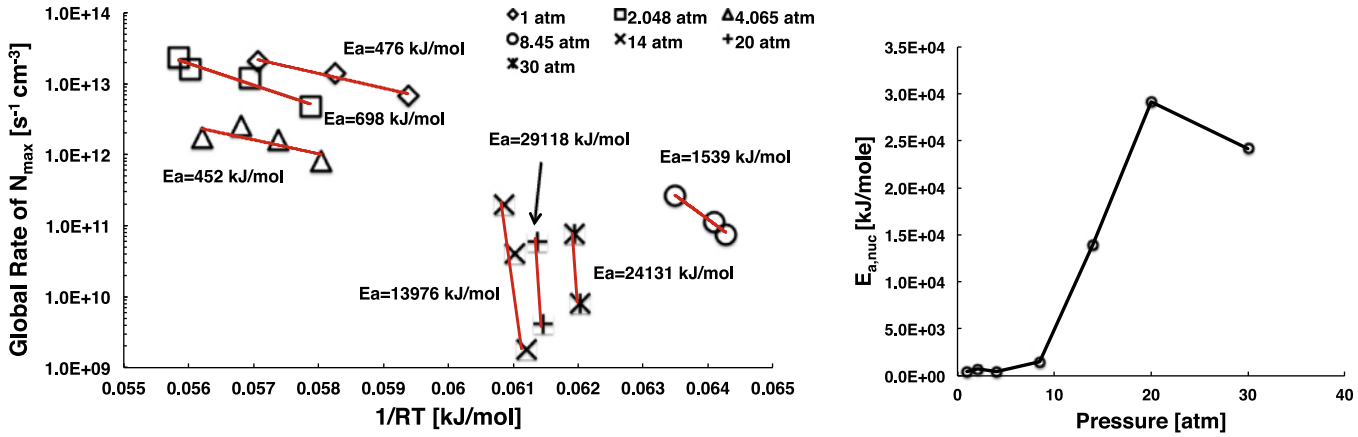

Fig. 12. (a) Global nucleation rate vs inverse peak flame temperature, with slope identifying the activation energy of soot nucleation rate, for all high-pressure experiments and (b) plot of the soot nucleation activation energy vs pressure.

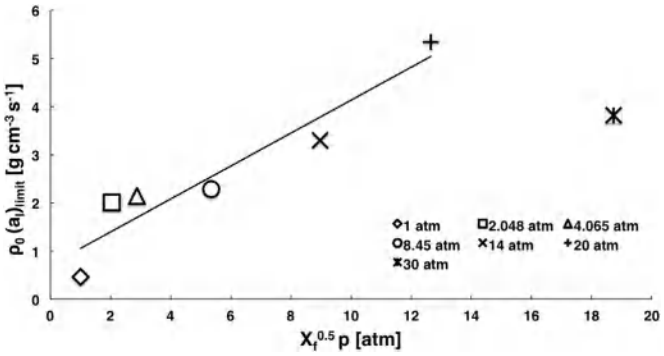

Fig. 13. Correlation between density weighted sooting strain rate vs fuel concentration/pressure.

Figure 12b shows a plot of the activation energy as a function of pressure. The activation energy is seen to increase exponentially up to about 20 atm, followed by sudden decrease. Increasing activation energy suggests a greatly increased sensitivity to temperature, implying that the nucleation will occur closer to the high temperature region of the flame with enhanced blackbody radiation emitted by soot particles. Further investigations are needed to verify the interesting trend observed here, specifically by conducting experiments at even higher pressures.

Based on limited ethylene-air non-premixed flame experiments in the range of 1 to 2.5 atm, Du et al. [32] have proposed a linear correlation between the sooting limit weighted with the density of the oxidizer stream $(\rho_o (a_l)_{limit})$ and $X_F^{0.5}$ p. Figure 13 shows that the present data mostly follows this correlation for the range of 1 to 20 atm, with the exception of the 30 atm data point. Clearly, higher pressure data are needed to verify the applicability of this interesting correlation and the accuracy of sooting limit at 30 atm.

7. Conclusions

A hybrid experimental and modeling approach was successfully implemented to analyze soot characteristics in counterflow non-premixed ethylene/oxygen/inert laminar flames up to 30 atm. In this approach, measured PIV boundary conditions were used in a counterflow flame solver to generate the necessary gas-phase temperature and other local physical–chemical properties required for LII analysis, while the measured LII signal and the temperature decay of soot particles via two-color pyrometry were used to extract local soot volume fraction and effective particle size.

Two key features implemented in this effort were: (i) minimization of LIF contributions with low laser fluences of approximately 0.1 J/cm^2 at a laser excitation wave length of 532 nm and analysis of the signal with 20 ns delay, and (ii) an absolute irradiance-calibrated LII approach for collecting quantitative soot incandescence signal. While the exact LIF contribution in present LII signal cannot be verified without using near IR excitation wave length, the measured soot volume fraction and particle diameter were found to be consistent with previously reported data. More importantly, the critical flow strain rate at which incipient soot appears (identified as the "sooting limit") was minimally affected, especially at high pressure.

Ethylene/oxygen/inert counterflow flame experiments were performed up to 30 atm while maintaining a maximum measured soot volume fraction of less than 8 ppm. This was accomplished by controlling the flow strain rate and dilution of both the fuel and the oxidizer stream. For pressures up to 8 atm, nitrogen gas was used as a diluent, while for pressures of 14 atm and higher, helium diluent was used to lower the Reynolds number below a critical value to maintain the flame in laminar mode. For each set of constant pressure experiments, the flame location (Z_{st}) within the mixing layer was held constant while the strain rate effects were explored, but due to varying levels of dilution at different pressures, the stoichiometric mixture fraction varied from 0.064 to 0.18. Despite such flame location variation effects, the analysis of high pressure data suggests that the global activation energy of soot nucleation increases exponentially with pressure, with a sudden drop around 20 atm. Further higher pressure experiments are needed to verify this interesting trend observed.

Acknowledgments

This work was supported by Rolls Royce and the Commonwealth Center for Aerospace Propulsion Systems, with Dr. MS Anand at Rolls Royce as the technical monitor. Authors wish to acknowledge Dr. Gaetano Esposito in assisting with flame structure calculations.

Appendix A. High-pressurecounterflow burner design

The pressure chamber of the counterflow burner was designed for a pressure of 200 atm with a maximum operational pressure of 50 atm, i.e., with a safety factor of four. The main chamber was carved out of a stainless steel (SS 303) block of 200 mm as shown

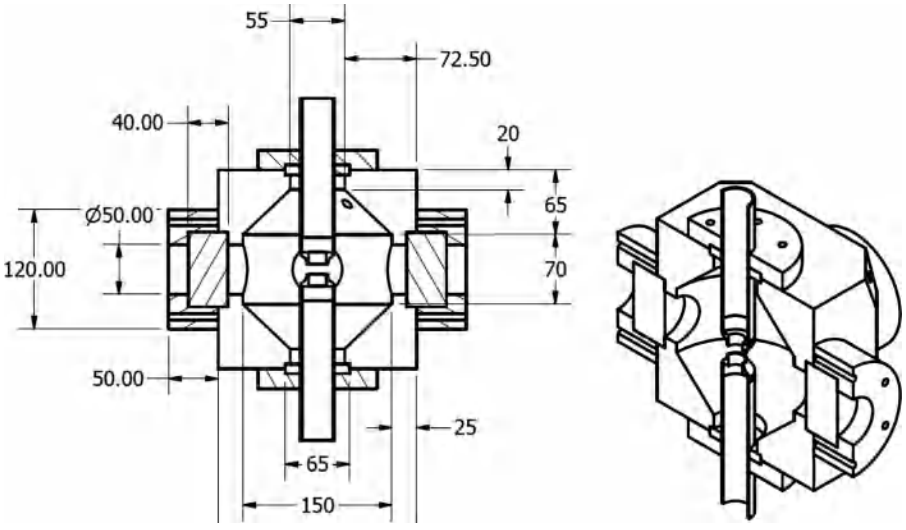

Fig. A.14. Cross-sectional and iso-metric views of the high-pressure chamber, with key dimensions, in mm.

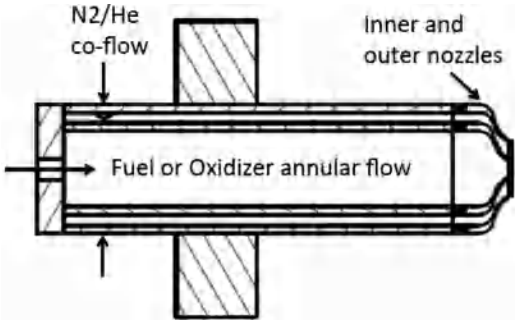

Fig. A.15. Cross-sectional view of the co-annular nozzle assembly (note: not to scale).

in Fig. A.14. The inner geometry of the chamber was comprised of a cylindrically-shaped region capped with two conical shape domes, and with four exhaust holes drilled from the top four edges of the block. The four side faces were designed to have optical access with fused silica windows, which were mounted using four flanges with an outer diameter of 120 mm, inner diameter of 50 mm, and a thickness of 40 mm. Each flange was mounted to the block using eight 3/8 inch bolts. The top and the bottom surfaces of the chamber have openings to insert co-annular flow tubes of either (i) fuel and inert or (ii) oxidizer and inert. The co-annular stainless steel flow tubes were identical, with outer and inner tubes connected via a flange as shown in Fig. A.15. Each outer tube was welded to a flange similar to those used to mount the optical windows, and was mounted to the main block using eight 3/8 inch bolts. Using aluminum blanks as windows, the entire assembly (i.e., chamber and the co-annular feed tubes) was hydrotested up to 200 atm.

Based on the stress analysis, the most sensitive components of the pressure chamber were the quartz windows. In addition to o-ring seals, flat gaskets were used to avoid direct metal-to-glass contact when assembling the windows. With such an arrangement, and with 75 mm diameter and 25 mm thick fused silica windows, the chamber was hydrotested up to 150 atm, yielding a desired safety factor of three at maximum operational pressure of 50 atm. Note: thus far LII data has been collected up to a pressure of 30 atm because of the current flow controllers are limited to a pressure of 34 atm.

Another important feature of the high-pressure counterflow burner was that the co-annular nozzle shape was designed to minimize Taylor-Görtler vorticity generation [47]. As shown in Fig. A.16, the calculated radial distance vs axial distance information were used in a NC controlled machine to fabricate the inner and outer nozzles, with an inner nozzle diameter of 6.5 mm. The separation distance between two nozzles was adjusted by inserting appropriate spacers between the nozzle assembly flange and the chamber. In the current setup, the separation distance was held constant at 5.45 mm. The alignment of the two opposed nozzle assembly was critical, and was facilitated by allowing for minor flexibility in flange bolt openings.

Appendix B. LII heat transfer model

Accurate determination of LII extracted quantities requires a heat transfer model of the heat exchange between a particle and its surrounding gas. The details of the LII heat transfer model and solution procedure have been extensively documented in previous work [51,52]. Since many research groups have employed slightly different approaches to LII heat transfer modeling, we list below only a summary of the specific governing equations and modifications relevant to this study. An assumption of particle aggregation is allowed in this formulation, and the common Rayleigh–Debye–Gans (RDG) approach is utilized as a modification to account for aggregation of primary soot particles. The governing equation relating the rate of change of internal energy of a nano-sized primary soot particle is given by,

$$\frac{dU_{internal}}{dt} = \dot{Q}_{absorption} - \dot{Q}_{radiation} - \dot{Q}_{sublimation} - \dot{Q}_{conduction}. \tag{B.1}$$

Here the right hand side terms are the rates of pulsed laser energy absorbed by the soot particle and heat lost via conduction, radiation, and sublimation heat transfer mechanisms. The above internal energy equation can also be written in terms of the rate of change of particle temperature ($T_{p,i}$), size (d_p), and mass (m_p). In particular, the rate of change of internal energy of the particle can be written as,

$$\frac{dU_{internal}}{dt} = \rho_s c_s \frac{\pi}{6} d_p^3 N_p \frac{dT_{p,i}}{dt}, \tag{B.2}$$

where ρ_s and c_s are the density and specific heat of soot, respectively, and N_p is the number of particles per aggregate where an aggregate or non-aggregated ($N_p = 1$) assumption can be made. The rate of pulsed laser energy absorbed by the particle is given by,

$$\dot{Q}_{absorption} = \frac{\pi^2 d_p^3 E(m) N_p}{\lambda_L} \frac{F_0 q(t)}{q_1}, \tag{B.3}$$

where the Rayleigh approximation for volumetric absorption by small particles (given $\pi d_p/\lambda_L < 0.3$) is assumed valid, $E(m) = -\mathrm{Im}\left[\frac{m^2-1}{m^2+2}\right]$ is the absorption function of soot at the laser wavelength λ_L, F_0 the laser fluence, and $q(t)/q_1$ the normalized laser temporal profile where integration over all time is equal to unity. A Gaussian temporal profile with a FWHM of 8 ns was assumed based on temporal profile measurements made on the laser used in this study. Absorption is assumed here to exhibit a $1/\lambda$ dependence in accordance with a majority of literature [58]. The rate of radiation heat transfer from Planck's law integrated over all wavelengths is given by,

$$\dot{Q}_{radiation} = \pi d_p^2 N_p \int_0^\infty \epsilon_\lambda \frac{2\pi hc^2}{\lambda^5[\exp(\frac{hc}{\lambda k_B (T_{p,i}-T)}) - 1]} d\lambda, \tag{B.4}$$

where

$$\epsilon_\lambda = 4\pi d_p E(m)/\lambda. \tag{B.5}$$

Here, the Rayleigh approximation for the emissivity ϵ_λ is assumed and is equal to the absorption efficiency under consideration of Kirchhoff's Law. Eq. (B.4) accounts for reabsorption of radiation at the local gas temperature T. The expression for the rate of heat loss due to sublimation is given by,

$$\dot{Q}_{sublimation} = -\frac{\Delta H_v}{W_v} \frac{dM}{dt}, \tag{B.6}$$

where

$$\frac{dM}{dt} = \frac{-\pi d_p^2 N_p W_v \alpha_M p_v}{R_p T_{p,i}} \sqrt{\frac{R_m T_{p,i}}{2\pi W_v}}, \tag{B.7}$$

$$p_v = p_{ref} \exp\left[-\frac{\Delta H_v}{R}\left(\frac{1}{T_{p,i}} - \frac{1}{T_{ref}}\right)\right]. \tag{B.8}$$

Here, W_v is the molecular weight of sublimed carbon, ΔH_v the enthalpy of formation of sublimed carbon, α_M the mass accommodation coefficient, p_{ref} and T_{ref} the reference pressure and temperature, and R, R_p, and R_m the universal gas constant expressed in different units. Conductive cooling of the soot particle to the surrounding gas is expressed by the Sherman model [59] in the transition regime,

$$\dot{Q}_{conduction} = \left[\frac{1}{\dot{Q}_C} + \frac{1}{\dot{Q}_{FM}}\right]^{-1}, \tag{B.9}$$

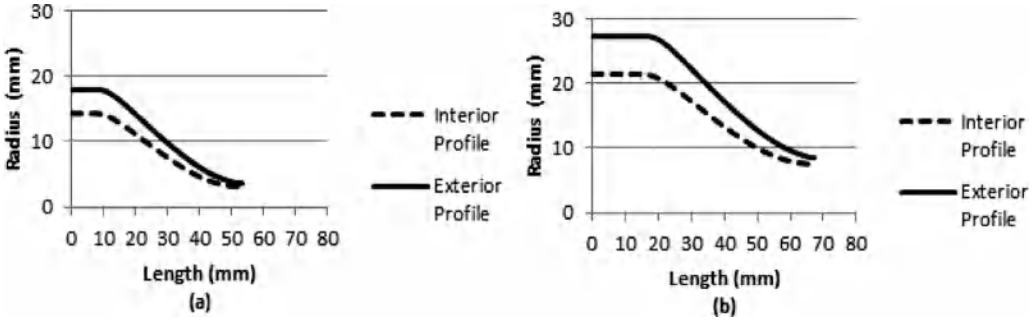

Fig. A.16. The shape of the nozzles (radius vs. distance), (a) inner nozzle and (b) outer nozzle.

where

$$\dot{Q}_C = 2\pi d_{eff}\kappa_h(T_{p,i} - T), \tag{B.10}$$

$$\dot{Q}_{FM} = \alpha_T \pi d_{eff}^2 \frac{p_0}{8}\frac{\gamma_h + 1}{\gamma_h - 1}\sqrt{\frac{8R_m T_g}{\pi \overline{W}}}\left(\frac{T_{p,i}}{T_g} - 1\right). \tag{B.11}$$

The validity and limitations of employing various conduction models are well documented (see [60] for an extensive review). $\dot{Q}_C$ is the continuum heat conduction rate, $\dot{Q}_{FM}$ is the free molecular heat conduction rate, κ_h is the harmonic mean thermal conductivity, γ_h the harmonic mean specific heat capacity ratio, p_0 the gas pressure, and $\overline{W}$ the molecular weight of the gas. In Eq. (B.10), the RDG theory is used to estimate an effective diameter d_{eff} due to partial shielding from particle aggregation as described by Brasil et al. [61]. This formulation differs from that commonly applied in literature, which uses a shielding relation based on 2D projected aggregate areas also proposed by Brasil et al. [61]. The original surface reduction relation adopted here has the added benefit of converging to the correct relation for particle diameter under the assumption of no aggregation i.e., $d_{eff} = d_p$. The equation d_{eff} adopted here is,

$$d_{eff} = d_p\sqrt{N_p\left[1 - \phi C_{ov}\left(1 - \frac{1}{N_p}\right)\right]}, \tag{B.12}$$

which can be related to two parameters; the fractal prefactor (k_f) and fractal dimension (D_f). A typical value of $D_f = 1.8$ is cited as common to many flame studies, with generally little variation [61]. The fractal prefactor k_f is more variable and dictates the extent of aggregate shielding through a primary particle overlap parameter,

$$C_{ov} = -0.0735k_f^2 + 0.5399k_f - 0.6398. \tag{B.13}$$

A fitting parameter ϕ (originally proposed as 1.3 by Brasil et al. [61]) was tuned to DSMC data for the effect of thermal accommodation on changes in aggregate surface shielding [62–64].

$$\phi = 1.7(0.7144\alpha_T + 0.2873) \tag{B.14}$$

The effective diameter due to aggregate shielding was assumed equal for the continuum and free molecular expressions used in the Sherman formulation for transition regime heat conduction. The coupled differential equations for changes in soot particle mass and temperature were solved using a fourth-order Runge–Kutta method and a time step of 400 ps.

Local variation in gas temperature and variations in the specific heat ratio, thermal conductivity, and molecular weight due to species concentrations and gas temperature were calculated using the Smooke's counterflow code [10] with a 56 species skeletal model extracted using a PCA procedure described in Esposito and Chelliah [65]. The temperature profiles calculated from the detailed

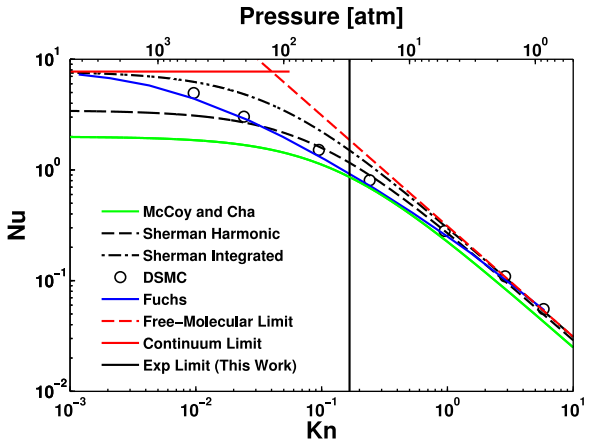

Fig. B.17. Nusselt numbers calculated from several heat conduction models including DSMC results by Liu et al. [60] for a range of Knudsen numbers and pressures at a gas temperature of 300 K.

model and the skeletal model at strain rates of interest were indistinguishable. Specifically, the thermal conductivity and heat capacity ratio as a function of temperature were fit to 2nd and 8th degree polynomials respectively and passed to the LII model to minimize processing time. In this work, harmonic mean heat transfer variables for thermal conductivity κ_h and specific heat capacity ratio γ_h evaluated at local gas temperature and particle temperature were employed. Liu et al. [60] recommended the use of Fuchs boundary sphere model with integrated mean heat transfer properties as a best fit to DSMC calculations of conduction heat transfer from a spherical particle. This approach requires iteration, however, a simpler non-iterative approach is desirable. Two heat transfer formulations, namely McCoy and Cha [66] and Sherman [59] models, match the requirement of a simple implementation without iteration. Figure B.17 shows the performance of several heat conduction models in terms of the Nusselt number as a function of the Knudsen number and pressure analyzed by Liu et al. [60], including DSMC results for a particle temperature of 3400 K, gas temperature of 300 K, and particle size of 30 nm. The Nusselt number corresponding to heat transfer was normalized by half the continuum heat transfer result with thermal conductivity of the surrounding gas evaluated at an ambient gas temperature of 300 K. The experimental limit of pressure in this work is 30 atm, represented by the black vertical line in Fig. B.17. Clearly the Fuchs approach suggested by Liu et al. and the Sherman approach with harmonic heat conduction properties are shown as equally valid for pressures up to 30 atm, and only show significant variation at several hundred atmospheres. Most notably, the McCoy and Cha model [66] exhibited persistent under prediction of the particle heat transfer rate across all pressures and was therefore ruled out. The harmonic Sherman

Table B1
Parameters for heat transfer model.

	Parameter	Description
Internal	ρ_s	$2.3031 - 7.3106 * 10^{-5}T$ [67]
	c_s	T-dependent [67,68]
Absorption and radiation	$E(m)$	0.3
	F	0.098–0.111 J/cm^2 peak
Sublimation	p_v	Clausius–Clapeyron equation [52,69]
	ΔH_v	T-dependent [52,69]
	W_v	T-dependent [52,69]
	α_m	0.8 [52]
Conduction	α_T	Local mixture averaged
	γ_h	$2/\left(\frac{1}{\gamma_{fg}} + \frac{1}{\gamma_T}\right)$
	κ_h	$2/\left(\frac{1}{\kappa_{fg}} + \frac{1}{\kappa_T}\right)$
	$\bar{W}$	Local mixture averaged
	D_f	1.8 [61] or calculated via TEM
	k_f	Calculated via TEM

approach was utilized in this work as an acceptable alternative to Fuchs formulation. Additional validations were conducted on the heat transfer model by comparing the formulation developed in this study against constrained and semi-constrained model comparisons in the literature [52]. All comparisons were in excellent agreement. The exact formulations for all relevant LII variables are listed in Table B1.

References

[1] A. Potter, S. Heimel, J. Butler, Apparent flame strength: a measure of maximum reaction rate in diffusion flames, Symp. (Int.) Combust. 8 (1960) 1027–1034.
[2] D. Spalding, Theory of mixing and chemical reaction in the opposed jet diffusion flame, ARS J. 31 (1961) 763–771.
[3] H. Tsuji, I. Yamaoka, The counterflow diffusion flame in the forward stagnation region of a porous cylinder, Symp. (Int.) Combust. 11 (1) (1967) 979–984.
[4] J. Kent, F. Williams, Extinction of laminar diffusion flames for liquid fuels, Symp. (Int.) Combust. 15 (1975) 315–325.
[5] K. Seshadri, F.A. Williams, Laminar flow between parallel plates with injection of a reactant at high Reynolds number, Int. J. Heat and Mass Transf. 21 (1978) 251–253.
[6] N. Peters, Laminar diffusion flamelet models in non-premixed turbulent combustion, Prog. Energy Comb. Sci. 10 (1984) 319–339.
[7] C. Law, D. Zhu, G. Yu, Propagation and extinction of stretched premixed flames, Symp. (Int.) Combust. 21 (1988) 1419–1426.
[8] F. Egolfopoulos, P. Cho, C. Law, Laminar flame speeds of methane-air mixtures under reduced and elevated pressures, Combust. Flame 76 (3) (1989) 375–391, doi:10.1016/0010-2180(89)90119-3.
[9] R.J. Kee, J.A. Miller, G.H. Evans, G. Dixon-Lewis, A computational model of the structure and extinction of strained, opposed flow, premixed methane-air flames, Proc. Combust. Inst. 22 (1) (1989) 1479–1494.
[10] M.D. Smooke, J. Crump, K. Seshadri, V. Giovangigli, Comparison between experimental measurements and numerical calculations of the structure of counterflow, diluted, methane-air, premixed flames, Symp. (Int.) Combust. 23 (1) (1991) 463–470, doi:10.1016/S0082-0784(06)80292-4.
[11] H.K. Chelliah, C.K. Law, T. Ueda, M.D. Smooke, F.A. Williams, An experimental and theoretical investigation of the dilution, pressure and flow-field effects on the extinction condition of methane-air-nitrogen diffusion flames, Symp. (Int.) Combust. 23 (1) (1991) 503–511, doi:10.1016/S0082-0784(06)80297-3.
[12] B.G. Sarnacki, G. Esposito, R.H. Krauss, H.K. Chelliah, Extinction limits and associated uncertainties of nonpremixed counterflow flames of methane, ethylene, propylene and n-butane in air, Combust. Flame 159 (3) (2011) 1026–1043, doi:10.1016/j.combustflame.2011.09.007.
[13] U. Niemann, K. Seshadri, F.A. Williams, Accuracies of laminar counterflow flame experiments, Combust. Flame 162 (4) (2015) 1540–1549, doi:10.1016/j.combustflame.2014.11.021.
[14] R. Johnson, A.C. Van Dine, G. Esposito, H.K. Chelliah, On the axisymmetric counterflow flame simulations: is there an optimal nozzle diameter and separation distance to apply quasi one-dimensional theory? Combust. Sci. Technol. 187 (2015) 37–59.
[15] U. Vandsburger, I.M. Kennedy, I. Glassman, Sooting counterflow diffusion flames with varying oxygen index, Combust. Sci. Tech. 39 (1–6) (1984) 263–285.
[16] I. Kennedy, Soot aerosol dynamics in a stagnation point diffusion flame, Symp. (Int.) Combust. 20 (1984) 1095–2204.
[17] D.X. Du, R. Axelbaum, C.K. Law, Experiments on the sooting limit of aerodynamically-strained diffusion flames, Symp. (Int.) Combust. 22 (1988) 387–394.
[18] H. Wang, D.X. Du, C.J. Sung, C.K. Law, Experiments and numerical simulation on soot formation in opposed-jet ethylene diffusion flames, Symp. (Int.) Combust. 26 (1996) 2359–2368.
[19] R.J. Hall, M.D. Smooke, M.B. Colket, Predictions of soot dynamics in opposed jet diffusion flames, in: F.L. Dryer, R.F. Sawyer (Eds.), Physical and Chemical Aspects of Combustion: A Tribute to Irvin Glassman, Gordon and Breach, Amsterdam (1997), pp. 189–230.
[20] K.T. Kang, J.Y. Hwang, S.H. Chung, W. Lee, Soot zone structure and sooting limit in diffusion flames : comparison of counterflow and co-flow flames, Combust. Flame 281 (1997) 266–281.
[21] K.C. Lin, G.M. Faeth, Structure of laminar permanently blue, opposed-jet ethylene-fueled diffusion flames, Combust. Flame 115 (1998) 468–480.
[22] N. Olten, S. Senkan, Formation of polycyclic aromatic hydrocarbons in an atmospheric pressure ethylene diffusion flame, Combust. Flame 118 (3) (1999) 500–507, doi:10.1016/S0010-2180(99)00004-8.
[23] J.Y. Hwang, S.H. Chung, Growth of soot particles in counterflow diffusion flames of ethylene, Combust. Flame 762 (2001) 752–762.
[24] S. Yoon, S. Lee, S. Chung, Effect of mixing methane, ethane, propane, and propene on the synergistic effect of PAH and soot formation in ethylene-base counterflow diffusion flames, Proc. Combust. Inst. 30 (1) (2005) 1417–1424, doi:10.1016/j.proci.2004.08.038.
[25] X. Zhu, J. Gore, Radiation effects on combustion and pollutant emissions of high-pressure opposed flow methane/air diffusion flames, Combust. Flame 141 (1) (2005) 118–130, doi:10.1016/j.combustflame.2004.12.012.
[26] K. Mcnesby, A. Miziolek, T. Nguyen, F. Delucia, R. Reedskaggs, T.A. Litzinger, Experimental and computational studies of oxidizer and fuel side addition of ethanol to opposed flow air/ethylene flames, Combust. Flame 142 (4) (2005) 413–427, doi:10.1016/j.combustflame.2005.04.003.
[27] S.H. Chung, A. Violi, Insights on the nanoparticle formation process in counterflow diffusion flames, Carbon 45 (12) (2007) 2400–2410, doi:10.1016/j.carbon.2007.07.003.
[28] A. D'anna, M. Commodo, M. Sirignano, P. Minutolo, R. Pagliara, Particle formation in opposed-flow diffusion flames of ethylene: an experimental and numerical study, Proc. Combust. Inst. 32 (2009) 793–801.
[29] Y. Wang, A. Raj, S.H. Chung, Soot modeling of counterflow diffusion flames of ethylene-based binary mixture fuels, Combust. Flame 162 (3) (2015) 586–596, doi:10.1016/j.combustflame.2014.08.016.
[30] P. Singh, X. Hui, C.-J. Sung, Soot formation in non-premixed counterflow flames of butane and butanol isomers, Combust. Flame 164 (2016) 167–182, doi:10.1016/j.combustflame.2015.11.015.
[31] S. Park, Y. Wang, S.H. Chung, S.M. Sarathy, Compositional effects on PAH and soot formation in counterflow diffusion flames of gasoline surrogate fuels, Combust. Flame 178 (2017) 46–60, doi:10.1016/j.combustflame.2017.01.001.
[32] D.X. Du, H. Wang, C.K. Law, Soot formation in counterflow ethylene diffusion flames from 1 to 2.5 atmospheres, Combust. Flame 270 (1998) 264–270.
[33] C.J. Sung, B. Li, H. Wang, C.K. Law, Structure and sooting limits in counterflow methane/air and propane/air diffusion flames from 1 to 5 atmospheres, Symp. (Int.) Combust. 27 (1998) 1523–1529.
[34] L. Figura, A. Gomez, Laminar counterflow steady diffusion flames under high pressure (P $\leq$ 3 MPa) conditions, Combust. Flame 159 (1) (2011) 142–150, doi:10.1016/j.combustflame.2011.06.013.
[35] F. Carbone, K. Gleason, A. Gomez, Pressure effects on incipiently sooting partially premixed counterflow flames of ethylene, Proc. Combust. Inst. 36 (1) (2017) 1395–1402, doi:10.1016/j.proci.2016.07.041.
[36] C.P. Leusden, N. Peters, Experimental and numerical analysis of the influence of oxygen on soot formation in laminar counterflow flames of acetylene, Proc. Combust. Inst 28 (2) (2000) 2619–2625, doi:10.1016/S0082-0784(00)80680-3.
[37] M. Yamamoto, S. Duan, S.M. Senkan, The effect of strain rate on polycyclic aromatic hydrocarbon (PAH) formation in acetylene diffusion flames, Combust. Flame 151 (2007) 532–541.
[38] R. Lindstedt, B. Waldheim, Modeling of soot particle size distributions in premixed stagnation flow flames, Proc. Combust. Inst. 34 (1) (2013) 1861–1868, doi:10.1016/j.proci.2012.05.047.
[39] R.L. Vander Wal, K.A. Jensen, M.Y. Choi, Simultaneous laser-induced emission of soot and polycyclic aromatic hydrocarbons within a gas-jet diffusion flame, Combust. Flame 109 (1997) 399–414.
[40] F. Ossler, T. Metz, M. Aldén, Picosecond laser-induced fluorescence from gas-phase polycyclic aromatic hydrocarbons at elevated temperatures. I. Cell measurements, Appl. Phys. B 72 (4) (2001) 465–478, doi:10.1007/s003400100519.
[41] M.S. Tsurikov, K.P. Geigle, V. Krüger, Y. Schneider-Kühnle, W. Stricker, R. Lückerath, R. Hadef, M. Aigner, Laser-based investigation of soot formation in laminar premixed flames at atmospheric and elevated pressures, Combust. Sci. Tech. 177 (10) (2005) 1835–1862, doi:10.1080/00102200590970212.
[42] F. Goulay, P. Schrader, L. Nemes, M.a. Dansson, H.A. Michelsen, Photochemical interferences for laser-induced incandescence of flame-generated soot, Proc. Combust. Inst 32 (1) (2009) 963–970, doi:10.1016/j.proci.2008.05.030.
[43] R. Sun, N. Zobel, Y. Neubauer, C.C. Chavez, F. Behrendt, Analysis of gas-phase polycyclic aromatic hydrocarbon mixtures by laser-induced fluorescence, Opt. Lasers Eng. 48 (12) (2010) 1231–1237, doi:10.1016/j.optlaseng.2010.06.009.
[44] G. Cléon, T. Amodeo, A. Faccinetto, P. Desgroux, Laser induced incandescence determination of e tio of e ot absorption functions at 532 nm and 1064 nm in e cleation zone of a low pressure premixed sooting flame, Appl. Phys. B 104 (2) (2011) 297–305, doi:10.1007/s00340-011-4372-z.
[45] S. Faust, G. Tea, T. Dreier, C. Schulz, Temperature, pressure, and bath gas composition dependence of fluorescence spectra and fluorescence lifetimes of toluene and naphthalene, Appl. Phys. B 110 (1) (2013) 81–93, doi:10.1007/s00340-012-5254-8.

[46] S. Bejaoui, X. Mercier, P. Desgroux, E. Therssen, Laser induced fluorescence spectroscopy of aromatic species produced in atmospheric sooting flames using uv and visible excitation wavelengths, Combust. Flame 161 (10) (2014) 2479–2491.
[47] J.M. Bergthorson, K. Sone, T.W. Mattner, P.E. Dimotakis, D.G. Goodwin, D.I. Meiron, Impinging laminar jets at moderate Reynolds numbers and separation distances, Phys. Rev. E 72 (2005). 066307–066301.
[48] H. Wang, E. Dames, B. Sirjean, D.A. Sheen, R. Tangko, A. Violi, J.Y.W. Lai, F.N. Egolfopoulos, D.F. Davidson, R.K. Hanson, C.T. Bowman, C.K. Law, W. Tsang, N.P. Cernansky, D.L. Miller, R.P. Lindstedt, A high-temperature chemical kinetic model of n-alkane (up to n-dodecane), cyclohexane, and methyl-, ethyl-, n-propyl and n-butyl-cyclohexane oxidation at high temperatures (jetsurf 2.0), Technical Report, Combustion Kinetics Laboratory, University of Southern California, 2011.
[49] G. Esposito, B.G. Sarnacki, H.K. Chelliah, Uncertainty propagation of chemical kinetics parameters and binary diffusion coefficients in predicting extinction limits of hydrogen/oxygen/nitrogen non-premixed flames, Combust. Theory Model. (2012) 1–24. November 2012 doi: 10.1080/13647830.2012.700406.
[50] H.A. Michelsen, P.O. Witze, D. Kayes, S. Hochgreb, Time-resolved laser-induced incandescence of soot: the influence of experimental factors and microphysical mechanisms., Appl. Opt. 42 (27) (2003) 5577–5590.
[51] C. Schulz, B.F. Kock, M. Hofmann, H.A. Michelsen, S. Will, B. Bougie, R. Suntz, G.J. Smallwood, Laser-induced incandescence: recent trends and current questions, Appl. Phys. B 83 (3) (2006) 333–354, doi:10.1007/s00340-006-2260-8.
[52] H.A. Michelsen, F. Liu, B.F. Kock, H. Bladh, a. Boiarciuc, M. Charwath, T. Dreier, R. Hadef, M. Hofmann, J. Reimann, S. Will, P.-E. Bengtsson, H. Bockhorn, F. Foucher, K.P. Geigle, C. Mounaïm-Rousselle, C. Schulz, R. Stirn, B. Tribalet, R. Suntz, Modeling laser-induced incandescence of soot: a summary and comparison of LII models, Appl. Phys. B 87 (3) (2007) 503–521, doi:10.1007/s00340-007-2619-5.
[53] D.R. Snelling, G.J. Smallwood, F. Liu, O.L. Gülder, W.D. Bachalo, A calibration-independent laser-induced incandescence technique for soot measurement by detecting absolute light intensity., Appl. Opt. 44 (31) (2005) 6773–6785.
[54] R. Santoro, H. Semerjian, R. Dobbins, Soot particle measurements in diffusion flames, Combust. Flame 51 (1983) 203–218, doi:10.1016/0010-2180(83)90099-8.
[55] L. Talbot, R.K. Cheng, R.W. Schefer, D.R. Willis, Thermophoresis of particles in a heated boundary layer, J. Fluid Mech. 101 (1980) 737.
[56] M. Frenklach, H. Wang, Detailed modeling of soot particle nucleation and growth, Symp. (Int.) Combust. 23 (1) (1991) 1559–1566, doi:10.1016/S0082-0784(06)80426-1.
[57] A.E. Karatas, O.L. Gülder, Soot formation in high pressure laminar diffusion flames, Prog. Energy Combust. Sci. 38 (6) (2012) 818–845, doi:10.1016/j.pecs.2012.04.003.
[58] T. Bond, R. Bergstrom, Light absorption by carbonaceous particles: an investigative review, Aerosol Sci. Tech. 40 (1) (2006) 27–67, doi:10.1080/02786820500421521.
[59] F.S. Sherman, A survey of experimental results and methods for the transition regime of rarefied gas dynamics, in: J.A. Lauermann (Ed.), Rarefied Gas Dynamics, Volume 2, Academic Press, New York (1963), p. 228.
[60] F. Liu, K.J. Daun, D.R. Snelling, G.J. Smallwood, Heat conduction from a spherical nano-particle: status of modeling heat conduction in laser-induced incandescence, Appl. Phys. B 83 (3) (2006) 355–382, doi:10.1007/s00340-006-2194-1.
[61] A.M. Brasil, T.L. Farias, M.G. Carvalho, A recipe for image characterization of fractal-like aggregates, J. Aerosol Sci. 30 (10) (1999) 1379–1389, doi:10.1016/S0021-8502(99)00026-9.
[62] K.J. Daun, Effect of selective accommodation on soot aggregate shielding in time-resolved laser-induced incandescence experiments, J. Heat Transf. 132 (9) (2010) 091202, doi:10.1115/1.4001614.
[63] A. Filippov, M. Zurita, D.E. Rosner, Fractal-like aggregates: relation between morphology and physical properties., J. Colloid Interface Sci. 229 (1) (2000) 261–273, doi:10.1006/jcis.2000.7027.
[64] F. Liu, M. Yang, F.a. Hill, D.R. Snelling, G.J. Smallwood, Influence of polydisperse distributions of both primary particle and aggregate size on soot temperature in low-fluence LII, Appl. Phys. B 83 (3) (2006) 383–395, doi:10.1007/s00340-006-2196-z.
[65] G. Esposito, H.K. Chelliah, Skeletal reaction models based on principal component analysis: application to ethylene-air ignition, propagation, and extinction phenomena, Combust. Flame 158 (3) (2011) 477–489, doi:10.1016/j.combustflame.2010.09.010.
[66] B.J. McCoy, C.Y. Cha, Transport phenomena in the rarefied gas transition regime, Chem. Eng. Sci. 29 (2) (1974) 381–388, doi:10.1016/0009-2509(74)80047-3.
[67] H.A. Michelsen, Understanding and predicting the temporal response of laser-induced incandescence from carbonaceous particles, J. Chem. Phys. 118 (15) (2003) 7012, doi:10.1063/1.1559483.
[68] L.E. Fried, W.M. Howard, Explicit Gibbs free energy equation of state applied to the carbon phase diagram, Phys. Rev. B 61 (13) (2000) 8734–8743.
[69] H. Leider, O. Krikorian, D. Young, Thermodynamic properties of carbon up to the critical point, Carbon 11 (5) (1973) 555–563, doi:10.1016/0008-6223(73)90316-3.